A Bi-Level Optimization Approach to Current Reference Configuration of IBRs in Modern Deregulated Distribution Systems

Tiantian JI[1], Pengfeng LIN[1], Haonan ZHU[1], Miao ZHU[1], Zhengmei LU[1], Yuwei SHANG[2]
[1]Department of Electrical Engineering, *Shanghai Jiao Tong University*, Shanghai, China
[2] *China Electric Power Research Institute*, Beijing, China
Email: thekiterunner@sjtu.edu.cn, linpengfeng@ieee.org, {zhn_kk6, miaozhu, luzhengmei}@sjtu.edu.cn, shangyuwei@epri.sgcc.com.cn

***Abstract*—In unbalanced grid scenarios, inverter-based resources (IBRs) should remain connected and inject reactive current to mitigate voltage unbalance at the point of common coupling (PCC). Although steady-state current reference generation is well-studied, transient issues like current overshoot and oscillation during reference switching remain overlooked. To bridge this gap, a bi-level current reference optimization approach is proposed. The dominant oscillatory modes of a grid-connected IBR system are first identified by closed-loop transfer function modeling. Then, a trajectory optimization problem is constructed in the frequency domain, where the current reference trajectory is reformulated by a virtual acceleration sequence (VAS). By maximizing the virtual energy of VAS under spectral energy constraints, the proposed method achieves fast and optimal reference transitions without exciting dominant modes. As a reference level strategy, it is fully compatible with existing controllers and adaptable to varying operating conditions. A complete design guideline is also provided. Dynamic simulations confirm the effectiveness of the proposed approach.**

***Index Terms*—Inverter-based resources, optimal trajectory, voltage unbalance, spectral energy constraint.**

I. Introduction

Voltage unbalance (VU) is a severe and widespread power quality issue, which becomes even more pronounced in modern power systems [1]. Recently, the widespread deployment of IBRs offers a new perspective on voltage unbalance attenuation (VUA). As a controllable current source, an IBR can inject a negative-sequence current (NSC) with a specific magnitude and phase angle into the grid, thereby realizing VUA at the PCC. We can leverage the spare capacity of IBRs to generate a compensating current, avoiding any additional hardware costs. There are two main types of IBR current reference generation methods. The first category employs the product of a fixed or adaptive droop coefficient and the negative-sequence voltage as the NSC reference [2]–[4]. The second category employs an optimization-based scheme [5]–[7]. In these optimization frameworks, the minimization of VUA is typically formulated as the objective, while physical constraints, including those on inverter capacity and output current, are treated as the problem's constraints. The model is then solved numerically to obtain a globally optimal current reference command.

However, there is a lack of research on the transient behavior of IBRs during current reference changes. Abrupt changes in the current reference serve as broadband excitations that may trigger the system's inherent oscillatory modes, particularly those with low damping ratios [8], [9]. The excitation of such modes often induces current overshoot and prolonged settling times. It may even cause instability if the system lacks sufficient damping. Practically, IBR control loops and relevant parameters are generally predefined and cannot be modified by system operators. Variations in system conditions may shift the dominant oscillation frequency, the preset damping becomes ineffective. While input shaping methods like low-pass filters are added to refine reference signals, they overly attenuate high-frequency components, unnecessarily sacrificing the system's dynamic response [10]–[12].

To achieve a faster possible transition without exciting underdamped oscillatory modes in a grid-connected IBR system, this paper proposes a bi-level current reference optimization approach. The upper level performs system modeling and eigen-analysis to identify the dominant oscillatory modes. In the lower level, a current reference trajectory (CRT) optimization problem is formulated in frequency domain to generate an optimal CRT (OCRT) that simultaneously ensures fast transitions while avoiding undesired mode excitation. At this level, the introduction of virtual acceleration and virtual energy reformulates CRT optimization into a more systematic framework, which improves convergence and simplifies modeling.

The remainder of this paper is organized as follows. Section II presents the upper level procedure for extracting the dominant modes. Section III develops the lower level formulation of the CRT optimization problem and the associated parameter selection. Section IV elaborates on the implementation details of the proposed approach, supported by dynamic simulations. Finally, Section V concludes the paper.

II. Upper Level for Dominant Modes Extraction

The VU at the PCC primarily arises from the unbalanced grid. The sequence extraction (SE) in Fig. 1 is implemented

This paper is supported by Smart Grid National Science and Technology Major Project under Grant 2025ZD0806600.

Corresponding author: Pengfeng LIN.

979-8-3315-8138-1

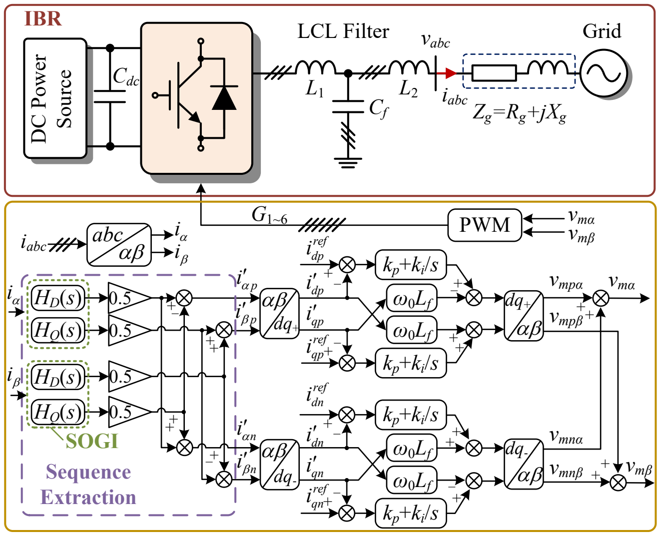

Fig. 1. Three-phase three-wire grid-tied system with dual sequence current control.

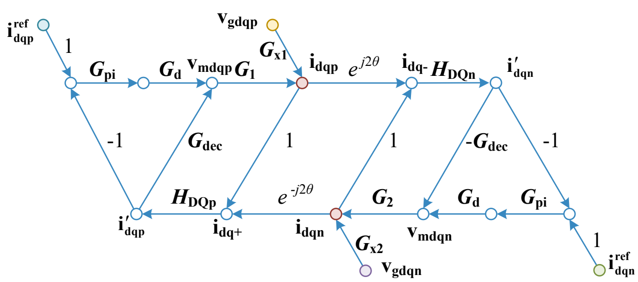

Fig. 2. Signal flow diagram of the studied system.

using a double second-order generalized integrator (SOGI). For the positive-sequence extraction branch in SE, the corresponding complex expression is given as (1). Subscripts "p/n" denote the positive- and negative-sequence components, respectively. These notations are used hereafter.

$$i'_{\alpha\beta p} = i'_{\alpha p} + j i'_{\beta p} = 0.5\left[H_D(s) + jH_Q(s)\right] i_{\alpha\beta} \tag{1}$$

where

$$H_D(s) = \frac{k\omega_0 s}{s^2 + k\omega_0 s + \omega_0^2},\ H_Q(s) = \frac{k\omega_0^2}{s^2 + k\omega_0 s + \omega_0^2}. \tag{2}$$

The Park transformation performs frequency spectrum shifting, i.e., $s_{dq\pm} = s_{\alpha\beta} \pm j\omega_0$. The subscripts "$dq+/dq-$" denotes the positive- and negative-sequence dq-frame, respectively. Accordingly, (1) can be rewritten as

$$i'_{dqp} = 0.5\left[H_D(s + j\omega_0) + jH_Q(s + j\omega_0)\right] i_{dq+} \tag{3}$$

By separating the real and imaginary parts, the purely real-valued matrix form of (3) in positive-sequence dq-frame is obtained, as shown in (4).

$$\begin{bmatrix} i'_{dp} \\ i'_{qp} \end{bmatrix} = \begin{bmatrix} H_{11p}(s) & H_{12p}(s) \\ H_{21p}(s) & H_{22p}(s) \end{bmatrix} \begin{bmatrix} i_{d+} \\ i_{q+} \end{bmatrix} = \boldsymbol{H}_{\mathbf{DQp}}\, \mathbf{i}_{\mathbf{dq+}} \tag{4}$$

where

$$\begin{cases} H_{11p}(s) = H_{22p}(s) \\ \quad = \dfrac{k\omega_0 s^3 + k^2\omega_0^2 s^2 + 4k\omega_0^3 s + 2k^2\omega_0^4}{2s^4 + 4k\omega_0 s^3 + (2k^2+8)\,\omega_0^2 s^2 + 8k\omega_0^3 s + 2k^2\omega_0^4} \\ H_{21p}(s) = -H_{12p}(s) \\ \quad = \dfrac{k^2\omega_0^3 s}{2s^4 + 4k\omega_0 s^3 + (2k^2+8)\,\omega_0^2 s^2 + 8k\omega_0^3 s + 2k^2\omega_0^4}. \end{cases} \tag{5}$$

Similarly, the expression for the negative-sequence extraction branch in SE within the negative-sequence dq-frame can be derived as

$$\begin{bmatrix} i'_{dn} \\ i'_{qn} \end{bmatrix} = \begin{bmatrix} H_{11n}(s) & H_{12n}(s) \\ H_{21n}(s) & H_{22n}(s) \end{bmatrix} \begin{bmatrix} i_{d-} \\ i_{q-} \end{bmatrix} = \boldsymbol{H}_{\mathbf{DQn}}\, \mathbf{i}_{\mathbf{dq\text{-}}} \tag{6}$$

where $\boldsymbol{H}_{\mathbf{DQn}} = \boldsymbol{H}_{\mathbf{DQp}}^{\boldsymbol{T}}$.

The quantity $\mathbf{i}_{\mathbf{dq+}}$ is obtained by directly applying the positive-sequence Park transformation to the $\mathbf{i}_{\alpha\beta}$. It contains the dc component and the second-harmonic coupled component. The same goes for $\mathbf{i}_{\mathbf{dq\text{-}}}$.

Fig. 1 is further transformed into the signal flow diagram in Fig. 2. The operator $e^{\pm j2\theta}$ represents the frequency shift between positive- and negative-sequence synchronous frames, i.e., $s_{dq\pm} = s_{dq\mp} \pm j2\omega_0$. The quantities in the two frames are coupled. Specifically, any variation in the positive-sequence current reference $\mathbf{i}^{\mathbf{ref}}_{\mathbf{dqp}}$ induces a transient response in the negative-sequence channel due to cross-coupling, and vice versa. These transient components eventually decay to zero. In Fig. 2, $\boldsymbol{G}_{\mathbf{pi}}$, $\boldsymbol{G}_{\mathbf{dec}}$ and $\boldsymbol{G}_{\mathbf{d}}$ denote the PI controller, current decoupling paths and control delay matrix, respectively, with explicit forms given in (7). The positive-sequence transfer function matrices of LCL filter are also given in (7). Accordingly, the negative-sequence matrices $\boldsymbol{G}_{\mathbf{L1n}}$, $\boldsymbol{G}_{\mathbf{L2n}}$, $\boldsymbol{G}_{\mathbf{Cn}}$, and $\boldsymbol{G}_{\mathbf{gn}}$ can be obtained by replacing ω_0 with $-\omega_0$ in the positive-sequence expressions.

$$\begin{cases} \boldsymbol{G}_{\mathbf{pi}} = \left(k_p + \dfrac{k_i}{s}\right)\boldsymbol{I}, & \boldsymbol{G}_{\mathbf{dec}} = \omega_0 L_f \begin{bmatrix} 0 & -1 \\ 1 & 0 \end{bmatrix}, \\ \boldsymbol{G}_{\mathbf{L1p}} = L_1\boldsymbol{P}, & \boldsymbol{G}_{\mathbf{Cfp}} = C_f\boldsymbol{P}, \\ \boldsymbol{G}_{\mathbf{L2p}} = L_2\boldsymbol{P}, & \boldsymbol{G}_{\mathbf{gp}} = L_g\boldsymbol{P} + R_g\boldsymbol{I}, \\ \boldsymbol{P} = [s,\ -\omega_0;\ \omega_0,\ s], & \boldsymbol{G}_{\mathbf{d}} = G_{del}\boldsymbol{I}. \end{cases} \tag{7}$$

The expressions of $\boldsymbol{G}_{\mathbf{1}}$, $\boldsymbol{G}_{\mathbf{x1}}$, $\boldsymbol{G}_{\mathbf{2}}$, and $\boldsymbol{G}_{\mathbf{x2}}$ shown in Fig. 2 are given as follows.

$$\begin{cases} \boldsymbol{G}_{\mathbf{1}} = \left[\left(\boldsymbol{I} + \boldsymbol{G}_{\mathbf{L1p}}\boldsymbol{G}_{\mathbf{Cp}}\right)\left(\boldsymbol{G}_{\mathbf{L2p}} + \boldsymbol{G}_{\mathbf{gp}}\right) + \boldsymbol{G}_{\mathbf{L1p}}\right]^{-1} \\ \boldsymbol{G}_{\mathbf{x1}} = -\left[\boldsymbol{G}_{\mathbf{L2p}} + \boldsymbol{G}_{\mathbf{gp}} + \boldsymbol{G}_{\mathbf{L1p}} + \boldsymbol{G}_{\mathbf{Cp}}^{-1}\right]^{-1} \\ \boldsymbol{G}_{\mathbf{2}} = \left[\left(\boldsymbol{I} + \boldsymbol{G}_{\mathbf{L1n}}\boldsymbol{G}_{\mathbf{Cn}}\right)\left(\boldsymbol{G}_{\mathbf{L2n}} + \boldsymbol{G}_{\mathbf{gn}}\right) + \boldsymbol{G}_{\mathbf{L1n}}\right]^{-1} \\ \boldsymbol{G}_{\mathbf{x2}} = -\left[\boldsymbol{G}_{\mathbf{L2n}} + \boldsymbol{G}_{\mathbf{gn}} + \boldsymbol{G}_{\mathbf{L1n}} + \boldsymbol{G}_{\mathbf{Cn}}^{-1}\right]^{-1} \end{cases}. \tag{8}$$

According to Mason's gain formula, the corresponding signal flow graph determinant equals

$$\Delta = \boldsymbol{I} + \boldsymbol{G}_{\mathbf{4}} - \boldsymbol{G}_{\mathbf{5}} - \boldsymbol{G}_{\mathbf{5}}\big|_{s=s+j2\omega_0}\boldsymbol{G}_{\mathbf{4}} + \boldsymbol{G}_{\mathbf{4}}\boldsymbol{G}_{\mathbf{5}}, \tag{9}$$

979-8-3315-8138-1

where

$$\begin{aligned}\boldsymbol{G}_4 &= \boldsymbol{G}_1\boldsymbol{G}_\mathbf{d}\left(\boldsymbol{G}_\mathbf{pi} - \boldsymbol{G}_\mathbf{dec}\right)\boldsymbol{H}_\mathbf{DQp},\\ \boldsymbol{G}_5 &= \boldsymbol{G}_2\boldsymbol{G}_\mathbf{d}\left(\boldsymbol{G}_\mathbf{pi} + \boldsymbol{G}_\mathbf{dec}\right)\boldsymbol{H}_\mathbf{DQn}.\end{aligned} \tag{10}$$

The transfer relations between the reference vectors and the actual dq currents are obtained by enumerating the forward paths and their corresponding cofactors. For the same sequence channels, the transfer matrices can be expressed as

$$\boldsymbol{T}_\mathbf{p} = \frac{l_1\Delta_1}{\Delta}, \boldsymbol{T}_\mathbf{n} = \frac{l_2\Delta_2}{\Delta} \tag{11}$$

where

$$l_1 = \boldsymbol{G}_1\boldsymbol{G}_\mathbf{d}\boldsymbol{G}_\mathbf{pi},\ \Delta_1 = \boldsymbol{I} - \boldsymbol{G}_5. \tag{12}$$

$$l_2 = \boldsymbol{G}_2\boldsymbol{G}_\mathbf{d}\boldsymbol{G}_\mathbf{pi},\ \Delta_2 = \boldsymbol{I} + \boldsymbol{G}_4. \tag{13}$$

The cross-sequence transfer relations are given by

$$\boldsymbol{T}_\mathbf{p2n} = \frac{l_3\Delta_3}{\Delta}, \boldsymbol{T}_\mathbf{n2p} = \frac{l_4\Delta_4}{\Delta} \tag{14}$$

where

$$l_3 = -\left(\boldsymbol{G}_1\boldsymbol{G}_\mathbf{d}\boldsymbol{G}_\mathbf{pi}\right)\big|_{s=s+j2\omega_0}\boldsymbol{G}_5, \Delta_3 = \boldsymbol{I}. \tag{15}$$

$$l_4 = -\left(\boldsymbol{G}_2\boldsymbol{G}_\mathbf{d}\boldsymbol{G}_\mathbf{pi}\right)\big|_{s=s-j2\omega_0}\boldsymbol{G}_4, \Delta_4 = \boldsymbol{I}. \tag{16}$$

Since the forward paths l_3 and l_4 contain frequency-shifted components, the corresponding references $\mathbf{i}_\mathbf{dqp}^\mathbf{ref}$ and $\mathbf{i}_\mathbf{dqn}^\mathbf{ref}$ should also undergo the same frequency offsets to maintain consistency. The obtained transfer function matrices are complex-valued. By separating the real and imaginary parts, their real-valued representations can be derived.

The overall transfer function matrices in positive- and negative-sequence dq-frame are expressed in (17). By analyzing the poles and zeros of these matrices, the dominant underdamped modes governing the system dynamics can be identified.

III. Lower Level for Current Reference Trajectory Optimization

A. Problem Formulation

Considering the finite sampling rate of practical digital control systems, the CRT is formulated as a discrete-time sequence. However, directly optimizing this sequence treats each sampling point as an independent variable without an underlying structure, which often leads to trajectories that are neither smooth nor convergent. To address this, the CRT is further modeled as a discrete signal that admits second-order differences, from which the concepts of virtual velocity, defined as the first-order difference of the CRT, and virtual acceleration, defined as the second-order difference, are introduced. By imposing spectral constraints on the virtual acceleration sequence (VAS) around the system's dominant mode frequencies, the corresponding spectral components in the CRT can be effectively suppressed, thereby avoiding undesired mode excitation.

Let $\boldsymbol{w} = [w_0, w_1, \ldots, w_{L-1}]^T$ denote the VAS of length L.The n-th FFT coefficient is given explicitly by (18). The frequency resolution is $f_{res} = f_s/L$. The frequency corresponding to W_n is $f_n = nf_{res}$.

$$W_n = \frac{1}{L}\sum_{k=0}^{L-1} w_k e^{-j\frac{2\pi nk}{L}}, \quad n \in [0, L-1]. \tag{18}$$

a) Mode Energy Constraints: Let the set of modes of interest be $\Omega = \{f^1, f^2, \ldots, f^M\}$, where f^m denotes the frequency of the m-th dominant mode, and M denotes the number of dominant modes. To mitigate the impact of model parameter inaccuracies, we introduced a frequency tolerance σ_t to achieve suppression over a frequency band rather than targeting a single frequency point. Accordingly, the forbidden band corresponding to the m-th mode is defined as (19).

$$F^m = \left[f^m - \sigma_t, f^m + \sigma_t\right]. \tag{19}$$

And the index set of FFT points of each F^m is given in (20).

$$\mathcal{N}^m = \{\, n \mid f_n \in F^m \,\}, \quad m \in [1, M]. \tag{20}$$

An auxiliary variable λ is introduced in (21) to represent the global maximum energy among all frequency points. The constraint in (22) then limits the total energy within each frequency band.

$$||W_n||^2 \le \lambda, \qquad \forall n \in [0, L-1]. \tag{21}$$

$$\sum_{n\in\mathcal{N}^m} ||W_n||^2 \le \rho\lambda, \quad \forall m \in [1, M]. \tag{22}$$

where $\rho \in (0, 1)$ is a suppression factor.

b) Initial-Final State Constraints: To guarantee a smooth and oscillation-free convergence of the CRT, the boundary conditions of the virtual velocity sequence are constrained as

$$v_0 = 0, \quad v_L = T_s\sum_{k=0}^{L-1} w_k = 0. \tag{23}$$

By integrating the above velocity constraints, the corresponding boundary condition of the CRT can be defined as

$$i_0 = 0, \quad i_{L+1} = T_s^2\sum_{k=0}^{L-1}(L-k)\, w_k = 1. \tag{24}$$

c) Objective: In the motion control field, the fastest transition between two positions with zero terminal velocity is a classical time-optimal control problem [13]. The optimal motion trajectory employs the maximum allowable acceleration, such that the system acquires the maximum possible energy from external actuation during the acceleration phase,

$$\begin{bmatrix}\mathbf{i}_\mathbf{dqp}(s)\\ \mathbf{i}_\mathbf{dqn}(s)\end{bmatrix} = \begin{bmatrix}\boldsymbol{T}_\mathbf{p}(s) & \mathbf{0}\\ \mathbf{0} & \boldsymbol{T}_\mathbf{n}(s)\end{bmatrix}\begin{bmatrix}\mathbf{i}_\mathbf{dqp}^\mathbf{ref}(s)\\ \mathbf{i}_\mathbf{dqn}^\mathbf{ref}(s)\end{bmatrix} + \begin{bmatrix}\mathbf{0} & \boldsymbol{T}_\mathbf{n2p}(s)\\ \boldsymbol{T}_\mathbf{p2n}(s) & \mathbf{0}\end{bmatrix}\begin{bmatrix}\mathbf{i}_\mathbf{dqp}^\mathbf{ref}(s - j2\omega_0)\\ \mathbf{i}_\mathbf{dqn}^\mathbf{ref}(s + j2\omega_0)\end{bmatrix}. \tag{17}$$

which is then dissipated during the deceleration phase. In this sense, acquiring maximum energy is equivalent to applying the largest admissible acceleration within the actuation limits. Inheriting this principle, the proposed formulation defines the virtual energy of VAS as $J(\boldsymbol{w}) = \|\boldsymbol{w}\|_2^2 = \boldsymbol{w}^T\boldsymbol{w}$.

Overall, the CRT optimization problem is formulated as (25). This problem is convex and can be solved by commercial optimization solvers. By double integration of the optimal VAS, the OCRT is obtained, which can be further scaled for application. The OCRT is held at its terminal value to provide a consistent input for the remaining time.

$$\begin{aligned} \max_{\boldsymbol{w}} \quad & J(\boldsymbol{w}) \\ \text{s.t.} \quad & (21)\text{–}(24). \end{aligned} \tag{25}$$

B. Parameter Design and Practical Implementation

i) σ_t design: For each dominant pole $p^m = -\sigma^m \pm j\omega^m$, its normalized spectral energy density is defined as $E^m(f) = |H^m|^2 / \int_0^{f_s/2} |H^m|^2 df$, where $|H^m(f)|^2 = [(\omega^{m2} - (2\pi f)^2 + \sigma^{m2})^2 + (4\pi f \sigma^m)^2]^{-1}$. σ_t^m is then determined such that (26) holds.

$$\int_{f^m-\sigma_t^m}^{f^m+\sigma_t^m} E^m(f)\, df \geq \eta, \tag{26}$$

where η is the energy coverage ratio. The unified tolerance σ_t is defined as the maximum among $\{\sigma_t^m\}_{m=1}^M$.

ii) L design: L is obtained via an iterative procedure. When $f_{res} = \sigma_t$, each mode band contains at least two FFT points, which is sufficient to ensure reliable optimization. Therefore, f_s/σ_t is selected as the upper limit L_{lim}. Subsequently, L can be gradually reduced from L_{lim} to find the smallest value that still yields satisfactory performance.

iii) Practical Implementation: The proposed optimization is conducted in an offline manner, where predefined tolerance margins are incorporated to account for parameter uncertainties. If a more accurate characterization of parameter uncertainty is required, Monte Carlo trails can be further employed to statistically evaluate its impact on the optimization results [14].

IV. Simulation Validation

System specifications and optimization parameters for simulation validation are summarized in Table I. The positive- and negative-sequence grid voltages are set to $V_{gp} = 217.7\angle 0°$V and $V_{gn} = 93.3\angle -30°$V, respectively. To achieve optimal VUA at PCC when the IBR output current is constrained, the current references are set to $I_{dp} = 19.19$A, $I_{qp} = -62.34$A, $I_{dn} = -15.53$A, $I_{qn} = -57.95$A based on the optimal NSC injection strategy described in our previous work [15].

Due to the structural symmetry of the system, the positive/negative sequence transfer function matrices and cross-coupling terms are identical, i.e., $\boldsymbol{T}_{\mathbf{p}} = \boldsymbol{T}_{\mathbf{n}}$ and $\boldsymbol{T}_{\mathbf{p2n}} = \boldsymbol{T}_{\mathbf{n2p}}$. Moreover, each of these transfer function matrices exhibits internal symmetry: the diagonal entries are identical, and the off-diagonal entries are negatives of each other. Therefore, only the Bode plots of $\boldsymbol{T}_{\mathbf{p}}(1,1)$, $\boldsymbol{T}_{\mathbf{p}}(1,2)$, $\boldsymbol{T}_{\mathbf{p2n}}(1,1)$, and $\boldsymbol{T}_{\mathbf{p2n}}(1,2)$ are drawn in Fig. 3. As can be observed, the resonance peaks are located at 50Hz, 836Hz, and 937Hz, corresponding to three dominant pole pairs $-31.8 \pm j314.2$, $-33.4 \pm j5247.5$, and $-46.9 \pm j5882.9$, respectively.

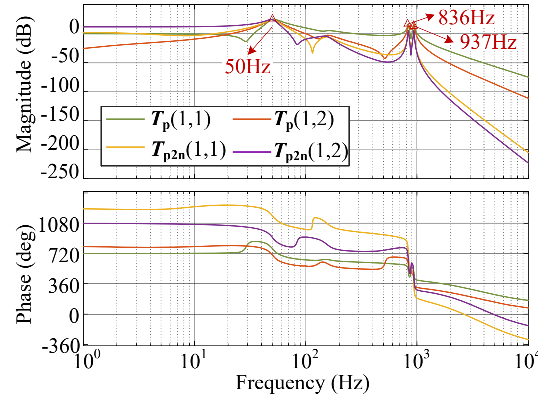

Fig. 3. Bode plots of $\boldsymbol{T}_{\mathbf{p}}(1,1)$, $\boldsymbol{T}_{\mathbf{p}}(1,2)$, $\boldsymbol{T}_{\mathbf{p2n}}(1,1)$, and $\boldsymbol{T}_{\mathbf{p2n}}(1,2)$.

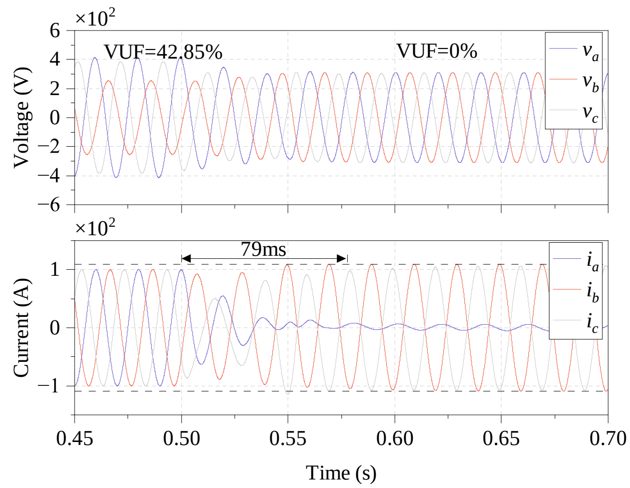

Fig. 4. OCRT responses of PCC voltage and output current under fault.

By applying the lower-level trajectory optimization process described earlier, a unit OCRT can be obtained and then amplitude-scaled to the desired current reference value. For comparison, three reference generation strategies are evalu-

TABLE I
System Specifications and Optimization Parameters

Description	Symbol	Value
DC-link voltage	V_{dc}	400V
Nominal AC voltage amplitude	V_g	311V
Maximum current limit	I_{lim}	110A
Nominal/Sampling frequency	f_0/f_s	50Hz/10kHz
Converter-side inductor of LCL filter	L_1	1mH
Capacitor of LCL filter	C_f	20μF
Grid-side inductor of LCL filter	L_2	2.5mH
Line resistance/inductance	R_g/L_g	1.1Ω/3.5mH
damping coefficient of SOGI	k	0.707
Current loop proportional/integral gain	k_p/k_i	10/400
Optimization horizon	L	450
Energy coverage ratio	η	80%
Frequency tolerance	σ_t	10Hz
Spectral suppression factor	ρ	0.0002

979-8-3315-8138-1

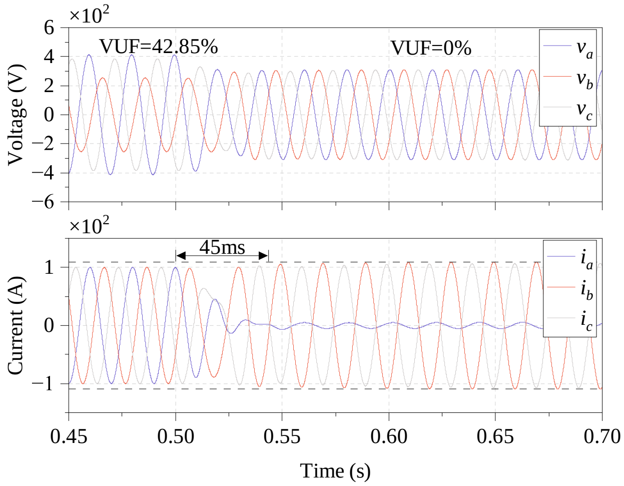

Fig. 5. Ramp responses of PCC voltage and output current under fault.

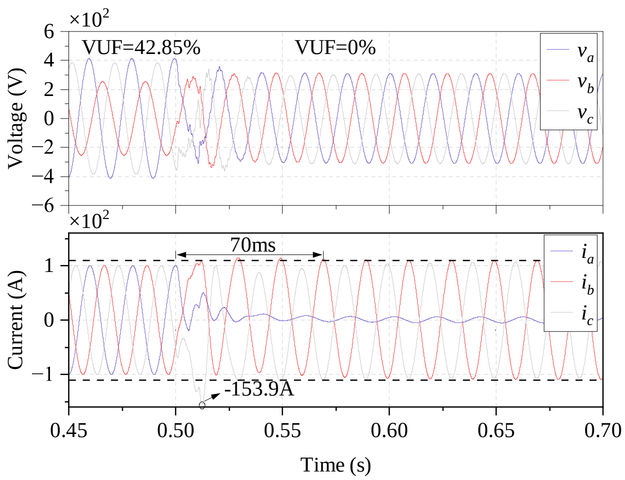

Fig. 6. Input shaping responses of PCC voltage and output current under fault.

ated, including the conventional ramp, the OCRT, and the input shaping approach implemented using the ZZVD shaper [10]. To ensure fairness, the ramp segment duration is matched to the length of the OCRT. Figs. 5–6 show the PCC voltage and output current responses under the OCRT, ramp and input shaping references, respectively. It can be observed that the ramp reference induces more pronounced oscillations during the transient process. In contrast, both the OCRT and ZZVD-based input shaping effectively suppress oscillatory behavior. In terms of transient recovery performance, the OCRT achieves the fastest settling, reaching steady state within 45 ms, whereas the ZZVD-based input shaping settles in 70 ms, and the ramp reference exhibits the slowest response with a settling time of 79 ms. At steady state, both methods achieve full VUA at the PCC once the NSC strategy is activated. These results indicate that the proposed trajectory optimization approach can be seamlessly integrated with the current injection strategy to achieve VUA at the PCC, while avoiding system oscillations during reference transitions.

V. Conclusion

This paper proposed a bi-level trajectory optimization approach for the current reference configuration of IBRs. By introducing the notions of virtual acceleration and virtual energy, the framework establishes an energy-based interpretation of trajectory dynamics. The incorporation of spectral energy constraints enables suppression of dominant oscillatory modes while maintaining fast transient performance. Moreover, the input–output transfer function model of the grid-connected IBR system is also provided. Dynamic simulations validate the effectiveness of the proposed approach.

References

[1] “Ieee standard for interconnection and interoperability of distributed energy resources with associated electric power systems interfaces,” *IEEE Std 1547-2018 (Revision of IEEE Std 1547-2003)*, pp. 1–138, 2018.

[2] P. Lin, Q. Meng, M. Zhu, A. M. Y. M. Ghias, and F. Blaabjerg, “Dynamic circuit-based unified power regulation for hybrid ac/dc/ds microgrids: A comprehensive approach to static and transient control,” *IEEE Transactions on Industrial Electronics*, pp. 1–12, 2025.

[3] C. Yang, T. Zheng, Y. Song, J. Hu, and J. M. Guerrero, “Coordinated control strategy of hybrid ac/dc microgrid for power quality improvement under unbalanced ac conditions,” *IEEE Transactions on Smart Grid*, vol. 16, no. 2, pp. 837–849, 2025.

[4] L. A. Budiwicaksana, T. Ardriani, J. Furqani, A. Rizqiawan, and P. A. Dahono, “Improving inverter output current controller under unbalanced conditions by using virtual impedance,” *IEEE Access*, vol. 9, pp. 162 359–162 369, 2021.

[5] A. Camacho, M. Castilla, J. Miret, L. G. de Vicuña, and R. Guzman, “Positive and negative sequence control strategies to maximize the voltage support in resistive–inductive grids during grid faults,” *IEEE Transactions on Power Electronics*, vol. 33, no. 6, pp. 5362–5373, 2018.

[6] Y. Guo, B. C. Pal, and R. A. Jabr, “On the optimality of voltage unbalance attenuation by inverters,” *IEEE Transactions on Sustainable Energy*, vol. 13, no. 3, pp. 1492–1506, 2022.

[7] B. R. Naidu, P. Bajpai, C. Chakraborty, M. Malakondaiah, and B. K. Kumar, “Adaptive dynamic voltage support scheme for fault ride-through operation of a microgrid,” *IEEE Transactions on Sustainable Energy*, vol. 14, no. 2, pp. 974–986, 2023.

[8] P. Lin, L. Du, H. Zhang, M. Zhu, J. Ma, and P. Wang, “Power lever: To transform interlinking architecture in hybrid ac/dc microgrids community,” *IEEE Transactions on Industrial Electronics*, pp. 1–14, 2025.

[9] D. Shi, P. Lin, Y. Wang, C.-C. Chu, Y. Xu, and P. Wang, “Deception attack detection of isolated dc microgrids under consensus- based distributed voltage control architecture,” *IEEE Journal on Emerging and Selected Topics in Circuits and Systems*, vol. 11, no. 1, pp. 155–167, 2021.

[10] L. Biagiotti and C. Melchiorri, *Trajectory planning for automatic machines and robots*. Springer Science & Business Media, 2008.

[11] T. Ji, P. Lin, M. Zhu, W. Jiang, X. Zhang, C. Wen, and P. Wang, “Mode-constrained two-stage current injection optimization for voltage unbalance mitigation in ibr-rich distribution network,” *IEEE Journal of Emerging and Selected Topics in Power Electronics*, pp. 1–1, 2025.

[12] C. Liyanage, L. Meegahapola, and I. Nutkani, “Post fault oscillation damping of power synchronisation control-based grid forming inverters,” *IEEE Transactions on Sustainable Energy*, pp. 1–18, 2025.

[13] R. Dorf and R. Bishop, *Modern Control Systems*. Pearson Prentice Hall, 2008. [Online]. Available: https://books.google.com/books?id=V-FpzJP5bEIC

[14] C. Song and R. Kawai, “Monte carlo and variance reduction methods for structural reliability analysis: A comprehensive review,” *Probabilistic Engineering Mechanics*, vol. 73, p. 103479, 2023. [Online]. Available: https://www.sciencedirect.com/science/article/pii/S0266892023000681

[15] T. Ji, P. Lin, C. Zhang, M. Zhu, and S. Wen, “Collaborative current injection optimization strategy of multiple inverter-based sources under unbalanced grid,” in *2025 IEEE Industry Applications Society Annual Meeting (IAS)*, 2025, pp. 1–5.

979-8-3315-8138-1